

Rydberg atoms in far-infrared radiation fields. I. Dipole matrix elements of H, Li, and Rb

J. H. Hoogenraad* and L. D. Noordam†

FOM Institute for Atomic and Molecular Physics, Kruislaan 407, 1098 SJ Amsterdam, The Netherlands

(Received 30 July 1997)

The radial electric dipole moments of bound-bound, bound-free, and free-free transitions of high-lying ($n > 15$) Rydberg states and low-lying continuum states ($\epsilon < 400 \text{ cm}^{-1}$) are calculated for hydrogen and the alkali-metal atoms. All dipole matrix elements for the transitions between low- l (s, p, d , and f) states of H, Li, and Rb are presented. Results of similar calculations for the other alkali-metal atoms (Na, K, and Cs) are summarized. These numerical results, using quantum defect theory, are compared with semiclassical approximations. The dipole matrix elements cross zero at certain combinations of initial and final states. The matrix elements at these so-called Cooper minima in Li, K, Rb, and Cs are presented in detail.

[S1050-2947(98)09605-X]

PACS number(s): 32.80.Rm, 32.70.Cs, 32.30.Bv

I. INTRODUCTION

Radiative transitions in Rydberg atoms are governed by the dipole matrix elements between high-lying states [1]. Dipole matrix elements between these states play an important role in many experiments: Transitions can be induced by collisions with charged particles [2–4], radiative recombination [5,6], irradiation with blackbody radiation [7–10], or by laser light [11,12]. The advent of tunable and intense far-infrared free-electron lasers opened a new class of laser-driven Rydberg-state experiments [13]. For a proper description of experiments on Rydberg atoms in far-infrared radiation fields [14–16], there is a need for the dipole matrix elements between Rydberg states. These matrix elements were so far not studied in this frequency range.

We have set out to calculate dipole matrix elements of bound-bound, bound-free, and free-free transitions of *high-lying* ($n > 15$) Rydberg states and low-lying continuum states ($\epsilon < 400 \text{ cm}^{-1}$) of the alkali-metal atoms, and tabulate the results. We present all the low- l dipole-allowed radiative transitions between 20 and 500 cm^{-1} (20 to $500 \mu\text{m}$) for hydrogen, lithium, and rubidium, and other alkali-metal atoms. Due to core interaction, the matrix elements of the alkali-metal atoms often deviate from hydrogenic approximations. The dipole matrix elements can either vanish or be enhanced, with sum rules only determining the *total* photoabsorption cross section [17]. Matrix elements for the transitions between *lower* Rydberg states ($n < 15$) and from these states into the continuum have intensively been studied [18,19].

Dipole matrix elements for photoabsorption can cross zero as a function of the final-state energy. The photoabsorption rate, proportional to the square of the dipole matrix element, vanishes at such a zero crossing, known as the Cooper minimum [20]. Similar minima are found in the photoexcitation of Rydberg states from the ground state of molecules [21–23]. The position of a Cooper minimum

changes if the initial state is an excited state [24–26]. Extending the range of n for the calculations, we found a number of Cooper minima in the high-Rydberg transitions of the alkali-metal atoms [13]. The Cooper minima are not reproduced in the most used analytical approximations [27] and a full numerical treatment of the problem is required.

In this paper we first introduce the main methods of calculation. We start with the separation of the wave function into angular and radial parts. The angular parts and their prefactors to the matrix elements are known, so that the remainder of the paper focuses on the radial parts of the wave functions. The numerical results for the radial matrix elements are compared with semiclassical matrix elements of hydrogen. Section II describes the semiclassical approximation, and the derived matrix elements. The computer code to evaluate the matrix elements numerically is described in Sec. III. In short, we calculate radial wave functions with a Numerov code, using quantum defect theory, and evaluate the matrix elements from these wave functions. In Secs. VI–IX, we present the calculations for a few elements: hydrogen, lithium, rubidium, and some transitions in potassium and cesium. For hydrogen, the semiclassical formulas agree with numerical calculations [27,28]. We present the results of our calculations for hydrogen as a reference to compare the results of the alkali-metal atoms. For lithium, the s - p transitions differ largely from the hydrogenic values: in the range of our calculations, a Rydberg bound-bound Cooper minimum occurs. We have chosen rubidium as a model alkali-metal atom. We present the matrix elements of all low- l transitions in Sec. VIII. Even though we have performed the calculations for all alkali-metal elements up to cesium, we only present the data for these elements to where anomalous behavior such as Cooper minima are found in the range of our calculations. Section X, finally, discusses some of the phenomena found in the calculations.

II. ANALYTICAL RESULTS

In the low-intensity limit, processes involving interaction with a single photon can be assigned a cross section. Within the rotating wave approximation, the cross section for photoionization is in atomic units,

*Present address: Philips Research Laboratories, Box WB-21, Prof. Holstlaan 4, NL-5656 AA Eindhoven, The Netherlands.

†Author to whom correspondence should be addressed.

$$\sigma_\omega = 4/3 \pi^2 \alpha \omega |\langle u_1 | \hat{z} | u_2 \rangle|^2 \equiv 4/3 \pi^2 \alpha \omega |\mathbf{D}|^2, \quad (1)$$

with ω the energy of the photons, α the fine structure constant, \hat{z} the direction of polarization of the electromagnetic field, u_1 and u_2 unperturbed wave functions, and \mathbf{D} the dipole matrix element.

The potential of any single-electron atom is spherically symmetric, and therefore the wave functions u can be divided into a radial part $R_{nl}(r)$ and an angular part $Y_{lm}(\theta, \phi)$

$$u = R_{nl}(r) Y_{lm}(\theta, \phi), \quad (2)$$

$$Y_{lm}(\theta, \phi) = \sqrt{\frac{(l-m)!}{(l+m)!} \frac{2l+1}{4\pi}} P_l^m(\cos\theta) e^{im\phi}. \quad (3)$$

The calculation of $\langle u_1 | \hat{z} | u_2 \rangle$ can also be factored into a radial and an angular part. The latter is calculated analytically, independent of the shape of the potential. Using the radial wave functions, the radial part of the dipole matrix element is expressed as

$$R_{n_1 l_1}^{n_2 l_2} = \int_0^\infty R_{n_1 l_1}(r) r R_{n_2 l_2}(r) dr. \quad (4)$$

The angular parts of the matrix elements \mathbf{D} give, for linearly polarized light, rise to the well known selection rules $\Delta_l = l_1 - l_2 = \pm 1$. The change of the magnetic quantum number m depends on the angle of the polarization of the light and the quantization axis of the atom. If both axes coincide, m is conserved, while in other cases also transitions occur in which m changes by plus or minus one.

For coinciding axes, the angular part of the dipole matrix element can be expressed as [17]

$$\langle l+1m | \hat{z} | lm \rangle = \langle lm | \hat{z} | l+1m \rangle = \sqrt{\frac{(l+1)^2 - m^2}{(2l+3)(2l+1)}}. \quad (5)$$

The calculation of the radial part of the matrix elements is more complicated. For hydrogen, exact analytical solutions for $R_{nl}(r)$ in terms of hypergeometric functions are known [29]. These functions, however, converge slowly for the highly excited states.

In the remainder of this section, we first describe approximations of the radial part of the hydrogenic matrix elements that can be made in various limiting cases. Differences of other elements with hydrogen can be modeled with a single parameter, the quantum defect, as described in Sec. II B. This does not yield simple semiclassical results for matrix elements involving a bound state. The matrix elements between two continuum states can be derived semiclassically, even for nonhydrogenic atoms. We give these free-free matrix elements in Sec. II C. The results of that section are used in the remainder of the paper as a reference for the calculated matrix elements.

A. Analytical matrix elements for H

Dipole matrix elements between loosely bound states of hydrogen can be approximated semiclassically with high accuracy. We use the results of the simplest of these calcula-

tions as a reference throughout the paper. We therefore start with introducing its background by briefly repeating the elegant derivation by Delone *et al.* [27].

It follows from the correspondence principle that dipole matrix elements equal the Fourier component at the transition frequency ω of the classical radial coordinate $r(t)$ of the Rydberg electron along its Kepler orbit:

$$\langle n' | r | n \rangle = \frac{1}{T} \int_0^T r(t) \cos \omega t dt. \quad (6)$$

The integration needs only be performed over one period ($T = 2\pi n^3$) of the classical orbiting time. For transitions between near-lying states, the transition frequency can be expressed as $\omega = (n' - n)/n^3$. In the half of the orbit where the electron moves away from the core, the trajectory of an electron on an outgoing $l=0$ orbit can be written as

$$r(t) = \frac{1}{2} (6t)^{2/3}. \quad (7)$$

Note that in this equation n is absent: The orbiting times of higher n states increase as n^3 , while the outer turning points (the maximal value of r) scale as n^2 . Substituting the half-orbit time in Eq. (7) yields the correct n dependence of the outer turning point. By substituting Eq. (7) into Eq. (6), the matrix element is

$$\langle n' | r | n \rangle = \frac{6^{2/3}}{T \omega^{5/3}} \int_0^{\pi(n'-n)} \phi^{2/3} \cos \phi d\phi. \quad (8)$$

As $n' - n$ is an integer, the integral takes values between 0.5 and 1. The integral converges slowly to its asymptotic value ($n' - n \rightarrow \infty$):

$$\langle n' | r | n \rangle \approx \frac{6^{2/3} \Gamma(\frac{2}{3})}{2\pi \sqrt{3} n^3 \omega^{5/3}}. \quad (9)$$

The two main characteristics of matrix elements between Rydberg states are present in this formula. First, the matrix elements are normalized to the density of states (n^{-3}), so that an integral over an interval of the spectrum is normalized. Secondly, the matrix elements depend on the transition frequency as $\omega^{-5/3}$: Transitions between nearby-lying states are favored over high-frequency transitions. The validity of Eq. (9) breaks down for transitions between neighboring states: No matrix element $\langle n' | r | n \rangle$ can be larger than the outer turning point ($2n^2$) of the lower state, while Eq. (9) has no upper bound. This limitation is only of importance for states within one n manifold: Eq. (9) yields already a smaller value of $0.4108n^2$ for $n \rightarrow n+1$ transitions ($\omega = n^{-3}$).

Equation (9) can be generalized further to remove the asymmetry of exchanging the initial n and final n' . We have reformulated the results of Goreslavskiĭ *et al.* [30] in terms of the binding energies of the states $\omega_n (= 1/2n^2)$ and $\omega_{n'}$ and the exact transition frequency $\omega = |\omega_{n'} - \omega_n|$:

$$\langle n' | r | n \rangle \approx C (-2\omega_{n'})^{3/4} (-2\omega_n)^{3/4} \omega^{-5/3}. \quad (10)$$

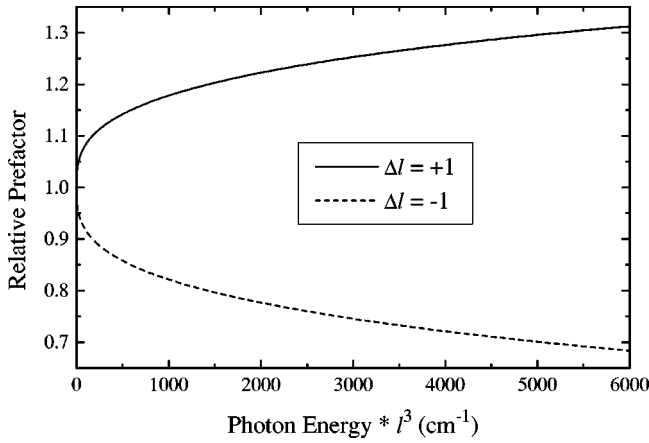


FIG. 1. Relative dipole matrix elements $C_+(\chi)/C(0)$ and $C_-(\chi)/C(0)$, calculated by the analytical formula Eq. (11) as a function of $l^3\omega$.

Again, the formula consists of three parts: The densities of states in the Rydberg series at states n and n' , a general frequency dependence, and a prefactor $C=0.4108$.

For transitions between states with angular momentum $l \neq 0$, Eq. (10) does not hold. The prefactor C , however, can be replaced by a frequency- and angular-momentum-dependent function. Inspired by Berson [31] we have rewritten the prefactor for low angular momenta and transition frequencies from [30]:

$$C_{\pm}(\chi) = \chi^{2/3} 3^{-1/2} / \pi [K_{2/3}(\chi) \pm K_{1/3}(\chi)], \quad (11)$$

with

$$\chi = l_{\max}^3 \omega / 3. \quad (12)$$

In Eq. (11), the deviations are expressed in Bessel- K , or McDonalds functions. The higher of the angular momenta of the two states is labeled l_{\max} . The + sign applies to $\Delta l = +1$ transitions in which the angular momentum of the higher-lying state is one unit more than the angular momentum of the lower state. Figure 1 shows $C_+(l^3\omega)$ and the corresponding $C_-(l^3\omega)$ function. At 4387 cm^{-1} , χ is only 0.02 a.u., and the requirement of small $l^3\omega$ for Eq. (11) is satisfied in the whole range of the figure. The prefactor reflects the Bethe rule: Transitions in which both the angular momentum and the energy are increased are more likely than those in which the angular momentum changes in the opposite direction. The difference becomes more pronounced as l increases: the higher l , the more the orbit resembles the classical Kepler orbit. For $l=m$ Kepler orbits, only the $\Delta l = +1$ transitions are classically allowed, as reflected in the higher matrix elements for these transitions for higher l . As Eq. (11) is only valid for low angular momenta and transition frequencies, we expand it in powers of χ :

$$C(0) = (4/3)^{1/3} / \Gamma(1/3) \approx 0.4108,$$

$$C_+/C(0) = 1 + 1.5702\chi^{1/3} - 1.5\chi - 1.1777\chi^{4/3} + O(\chi^2), \quad (13)$$

$$C_-/C(0) = 1 - 1.5702\chi^{1/3} + 1.5\chi - 1.1777\chi^{4/3} + O(\chi^2).$$

C_+ and C_- have the same value for $\chi=0$, which is the same as we derived for the $l=0$ dipole matrix elements. Normalized to this value, the two series expansions correspond to the values in Fig. 1. The functions start symmetrically from $\chi=0$. After the initial increase, C_+ will also decrease as a function of χ : Matrix elements for higher-angular-momentum states are smaller than those for lower-angular-momentum states.

The first term in Eq. (13) for the $\Delta l = +1$ transitions agrees with recent analytical calculations [32]. Reference [32], however, neither includes higher-order terms, nor describes the $\Delta l = -1$ transitions.

B. Quantum-defect theory for nonhydrogenic atoms

Quantum-defect theory (QDT) [33,34] is a generalization of the hydrogenic methods. QDT wave functions of excited states are calculated in the Coulomb potential at energies determined from experimental data. At large distances, the exact potential is indistinguishable from a Coulomb potential. Most of the wave function of highly excited, and high-angular-momentum states, is at these large distances so that QDT provides an excellent description. In QDT, deviations from hydrogenic eigenenergies are described with a change in effective quantum number: The energy levels are thus defined to be $1/[2(n-\mu_l)^2]$, with μ_l the quantum defect. For high n , μ_l is constant, but decreases with angular quantum number, as the centrifugal barrier reduces core penetration.

Analytical methods for calculation of hydrogenic wave functions and matrix elements can in principle be used for QDT: Both the f - and the g -wave functions can be expressed in Bessel functions, and (somewhat cumbersome) expressions for the dipole matrix elements are found [35]. The matrix elements are nearly hydrogenic whenever the quantum defects are small. In that case Eq. (10) and Eq. (11) can be used. The matrix elements strongly deviate from Eq. (10) as a function of the quantum defect. Even Eq. (8) has this property: At $n+1/2$, the integral yields near-zero values. If matrix elements are expanded in a series in the difference in the effective quantum number n^* of the states, this periodicity becomes clear: The coefficients can be described as Anger functions [28]. Values of these functions are tabulated for $\Delta n^* < 5$ in Ref. [36]. The matrix elements depend critically on the evaluation of these functions. For larger differences Δn^* , the functions become difficult to evaluate. Therefore we have chosen to generate the wave functions numerically, and calculate dipole matrix elements from them.

C. Matrix elements of continuum states

Within quantum-defect theory, one can derive matrix elements between two continuum states. The quantum defect is then interpreted as the phase shift that the wave function undergoes in scattering with the core. The hydrogenic continuum wave functions can be phase shifted to represent quantum defect wave functions of alkali-metal atoms. The scattering amplitudes depend on the difference in quantum defects of the two states: $\Delta_l = \pi(\mu_{l'} - \mu_l)$, where $l' < l$, so that Δ_l is positive. In this section, we present matrix elements for three regimes of the transition frequency ω relative to the average energy of the free states, $E = \frac{1}{2}(\epsilon + \epsilon')$.

Whenever $\omega \ll E$, free-free matrix elements increase rapidly when the energy difference of the two states reduces. For low l , the free-free matrix elements can be expressed as [37,38]

$$\langle \epsilon' l' | r | \epsilon l \rangle = \sqrt{\frac{2E}{\pi \omega^2}} \cos \Delta_l. \quad (14)$$

For $\omega > E$, free-free matrix elements become similar to the semiclassical formula. Equation (10) is easily continued over the threshold by replacing the prefactors for the density of states with 1 for any free state [30]. Delone *et al.* [37] have derived that the quantum defect difference can be included, so that the complete formula reads

$$\langle \epsilon' l' | r | \epsilon l \rangle = \frac{0.4744}{\omega^{5/3}} \cos(\Delta_l \pm \pi/6). \quad (15)$$

The sign in this expression depends on the sign of the momentum change: $\Delta l = +1$ transitions have the + sign. Equation (15) agrees with Eq. (10) when $\Delta_l \ll \pi/6$. Equation (15), however, does not reflect the Bethe rule, and when the quantum defect differences are small, Eq. (11) yields better results.

The transition from the regime where Eq. (14) holds to the regime where Eq. (15) is valid, at $\omega \sim E$, can be described by a complicated formula [37,38]. The onset of Eq. (14) for low transition frequencies is analogous to the breakdown of Eq. (9) for $n \rightarrow n+1$ bound-bound transitions.

III. ALGORITHMS

We have numerically calculated quantum defect wave functions and evaluated dipole matrix elements for combinations of states. This section describes the principles of the computer program.

For bound states, we follow a standard procedure, where the quantum defect is introduced by shifting the energy at which the wave function is calculated in a Coulomb potential. For continuum states, the quantum defect must be included by phase shifting the wave function, as described in Sec. III B. All wave functions in one run are calculated at radial coordinates on the same grid. The choice of the grid is explained in Sec. III C. After the calculation of the wave functions, the dipole matrix elements are calculated using the algorithms presented in Sec. III D. Finally, we tabulate the quantum defects in Sec. III E.

A. Bound wave functions

For bound-bound transitions, we used a standard Numerov integration [39] to generate the radial wave functions: Wave functions are calculated by integrating inwards from just outside the outer turning point ($r = [-1 - \sqrt{1 + 1/\omega_n l(l+1)}]/2\omega_n$) [18]. In the classically forbidden region, the physical wave function increases exponentially while integrating inwards and small components of the exponentially decreasing other solution damp out. The integration is stopped at 90% of the inner turning point ($r = [-1 + \sqrt{1 + 2/\omega_n l(l+1)}]/2\omega_n$), or whenever the wave function starts to increase again near the core. We have verified that

the results do not depend on this cutoff. The resulting wave functions are normalized afterwards.

B. Continuum wave functions

For continuum wave functions, the outer boundary condition cannot as easily be used as a starting value. To generate continuum wave functions, we used the method of Spencer *et al.* [40]. First, a hydrogenic wave function is calculated, starting from the core. If the wave function has a nonzero quantum defect, the phase of this hydrogenic solution is determined at R_{\max} . The wave function is phase shifted by π times the quantum defect. This phase, and the amplitude [given by the normalization $\sqrt{2/\pi}(2E)^{-1/4}$], provide the initial conditions for the same inward integration as for the bound wave functions.

C. Choice of grid

The calculation of wave functions is performed on a grid of radial coordinates. Ideally, the number of grid points is adapted to the distance between the nodes of the wave function. However, the behavior of the wave function dictates different grids in two spatial regions: Near the core, where the energy is mainly determined by the core potential, a logarithmic grid serves this goal best [39], while for continuum states far away, the distance between the nodes is nearly constant, and a linear grid is preferred. A fair solution is to calculate the wave function on blocks of linear grid, with increasing density of points when approaching the core [24]. Another approach is a grid that slowly changes from logarithmic to linear [19,41]: $x = \alpha r + \beta \ln r$, with r the grid index. We have chosen a grid which consists of a logarithmic part near the core, and a linear part far away. This grid is set up before the calculation and is equal for all states.

The lowest continuum state (at E_{\min}) determines the maximal radius on the grid. All continuum wave functions are calculated up to this radius

$$R_{\max} = ZF_{\text{end}}/E_{\min}. \quad (16)$$

Z , the charge of the core, is 1 and F_{end} is typically 20. The grid indices are generated by either of these two expressions:

$$r[i-1] = r[i]A \quad \text{logarithmic}, \quad (17)$$

$$r[i-1] = r[i] + S_{\text{lin}} \quad \text{linear}. \quad (18)$$

The logarithmic part of the grid is determined by the fixed parameter A (typically $e^{0.003}$). The most rapid oscillations of the wave function on the linear grid occur near the matching point with the logarithmic grid. The linear step size is chosen such that a minimal number of points per node (N_{\min} , typically 20) at the matching point is guaranteed for the highest energy E_{\max} of any continuum state in the calculation. The linear and logarithmic grid spacings determine the point where the logarithmic step size equals the linear step size. The grid is set up from that point, so that the first linear step is also a valid logarithmic step. R_{\max} and S_{lin} determine the number of grid points in the linear part of the grid. The remaining part of the total buffer of 60 000 points is used for the logarithmic part.

The wave functions were rewritten into Numerov form by transforming the wave functions by

$$y[i] = R[i] \sqrt{r} = \rho / \sqrt{r} \text{ logarithmic,} \quad (19)$$

$$y[i] = R[i] = \rho / r \text{ linear.} \quad (20)$$

In the linear regime, the solved differential equation is just the Schrödinger equation, while a transformation [39] is used in the logarithmic regime.

For integrating bound states inwards, the initial condition of the wave function corresponds to an increasing exponential. The outward integration of hydrogenic free states always starts on the logarithmic grid. We use the expansion of the f functions for $r \rightarrow 0$ and Eq. (20) and start the buffer with $y[i] = y[i+1]A^{(l+0.5)}$.

D. Matrix element calculation

The integral in Eq. (4) is evaluated using the generated wave functions. The multiplications are performed before Simpson's rule is used for the integration. In the integration of the logarithmic part, r is used as the additional Jacobian factor, and the result is divided by the logarithm of the step size AX .

For the free-free matrix elements, Eq. (4) involves integrating a rapidly oscillating and diverging function of r . The contributions from this region, where the potential is negligible compared to the energy of the state, must integrate to zero. The wave functions can be truncated to the region near the core by applying a filter function that depends on the local wave vector [42]. First, the integrand of Eq. (4) is mapped onto a linear grid with step size S_{lin} for the entire r range. Then, two digital filters are applied, with zeros at the asymptotic sum and difference of the wave vectors. Two three-point digital filters are applied six times, to damp the oscillations far away from the core [42]. Unfortunately, this reduced the usable range in r by the size of the filter functions. This size ($\sim 18 \times [1/(k_1 + k_2) + |1/(k_1 - k_2)|]$) sets the lower-energy limit on transitions we could integrate accurately.

We verified the algorithms by comparing the results with calculations that only included bound states. A completely logarithmic grid was used in those calculations, so that problems with the matching of the grids, the quantum defect shifting, and the filtered matrix element calculations could be verified by requiring continuity over the ionization threshold.

E. Quantum-defect extrapolation

Even though quantum defects change little as a function of n , agreement with the binding energies of very low-lying states can be achieved with an interpolating polynomial, for which coefficients are tabulated [43]. We have extrapolated the same polynomial over the ionization threshold to obtain the quantum defects in the continuum:

$$\mu_l(E_0) = \sum_k (-2E_0)^k T_{l,k}. \quad (21)$$

For bound states, the initial value for the energy is $E_0(n, l) = -\frac{1}{2}(n - T_{l,0})^{-2}$.

TABLE I. First-order terms $T_{l,0}$ to the quantum defects of the alkali-metal atoms, averaged over the fine-structure levels (from [43]).

	s	p	d	f
Li	0.399	0.047	0.002	0.0003
Na	1.348	0.855	0.016	0.0017
K	2.180	1.712	0.277	0.0101
Rb	3.131	2.648	1.347	0.0163
Cs	4.049	3.575	2.471	0.0335

The first-order terms to the quantum defects, which dominate for high n , are listed in Table I. As the size of the core increases for the heavier elements, the quantum defect increases. The fractional part of the quantum defect is the most important. An increase of the quantum defect with an integer merely changes the effective n , but does not affect the relative phase of the wave functions.

Quantum defects can also be used to parametrize the fine structure splitting. A small change in the first-order quantum defect term $T_{l,0}$ causes an energy shift for Rydberg states that scales with n^{*3} , in agreement with the splitting scaling with the overlap with the core [1].

The quantum-defect parameters in Table I are the average of the two fine-structure levels. Table II shows the differences in quantum defects of the fine-structure levels of the alkali-metal atoms, and the corresponding parameter for hydrogen. We encounter the influence of the fine-structure splitting on the matrix elements for the heavier alkali-metal atoms.

IV. NORMALIZATION OF THE PRESENTED MATRIX ELEMENTS

In the remainder of this paper, we present all matrix elements as a fraction of the simplest semiclassical formula, Eq. (10) with $C = 0.4108$. The tabulated values will therefore be

$$V = \frac{\langle n' | r | n \rangle_{\text{calc}}}{0.4108 (-2\omega_{n'})^{3/4} (-2\omega_n)^{3/4} \omega^{-5/3}}. \quad (22)$$

We present matrix elements for transitions with ω varying a factor 20. The details of the matrix element sizes had been invisible in the variations of ω , if the unscaled matrix elements would have been given. For continuum initial and final states, the $(-2\omega_{n,n'})^{3/4}$ factors are set to 1. Due to this choice, V passes smoothly over the ionization threshold.

TABLE II. Splitting of the first-order terms $T_{l,0}$ due to fine structure (from values compiled in [1]).

	p	d	f
H	1.333×10^{-5}	4.44×10^{-6}	2.22×10^{-6}
Li	1.133×10^{-5}	4.42×10^{-6}	
Na	0.0008174	-1.49×10^{-5}	2.16×10^{-6}
K	0.0003054	-0.00017	
Rb	0.0130561	0.0016422	-2.31×10^{-5}
Cs	0.0325281	0.0091564	-0.000149

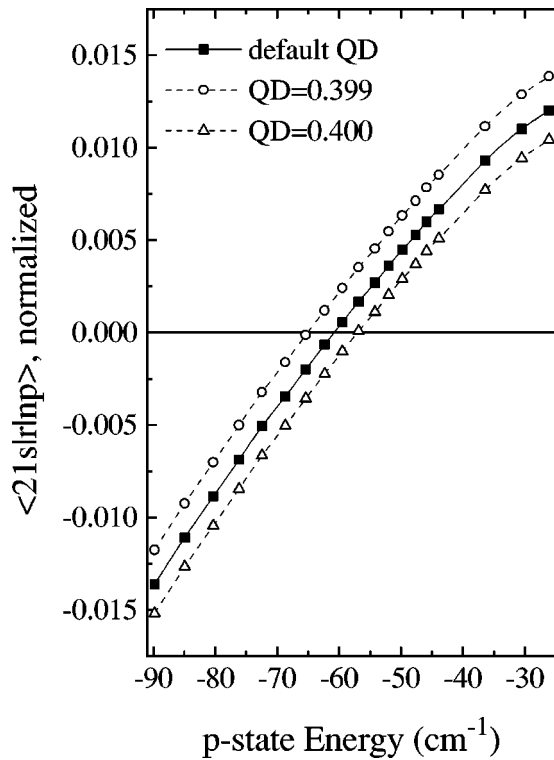


FIG. 2. Li $21s$ - np relative dipole matrix elements, normalized as in Eq. (22). Markers show the positions of the individual $35p$ - $50p$ states, and a few higher-lying states. The three curves show results for three quantum defect values of the $21s$ state: the middle the correct one, and the other two deviating values.

Most data will be presented as contour plots, with contours chosen to represent the dynamical range of any individual graph best. For rapid comparison, a gray scale is added that scales with $|V|$, and is common to all graphs. The approximate magnitudes of matrix elements (and thus the transition rates) can therefore be compared easily between the elements.

V. ACCURACY

The accuracy of the calculations could be determined by the following parameters: the accuracy of the potential used, the choice of the inner turning point, the quantum defects used, the grid size, and computer accuracy. For calculations involving only bound states, the grid size could be chosen arbitrarily, and convergence was found for a wide range of step sizes, the smallest size determined by the Pentium-based computer used for the calculations. By verifying smoothness over the threshold, the bound-free matrix elements were similarly verified not to depend on the grid size. The dependence on model parameters was checked at one of the most sensitive points in the calculation: a Cooper minimum in the high-lying bound-bound Rydberg transitions. Figure 2 shows the matrix elements between the Li $21s$ state and higher-lying p states, normalized as in Eq. (22). We have used the exact Coulomb potential. The inaccuracies in the potential are the position of the inner turning point and the quantum defect. The inner turning point dependence was checked by integrating the wave functions only over the outer range of the grid (the wave functions are calculated inwards, and are

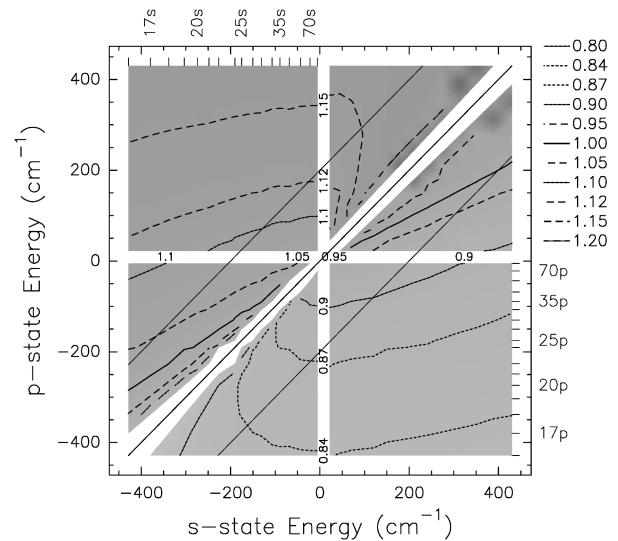


FIG. 3. Hydrogen s - p relative dipole matrix elements, normalized as in Eq. (22). Diagonals show $\omega = 200 \text{ cm}^{-1}$. For the conversion to cross sections, see Sec. VI.

thus independent of the inner turning point). The part of the integral from 0.5 to 5 a.u. does not contribute to the matrix element. Integrating from 10 a.u. (far outside the two-electron Li core) instead of starting from 0.5 a.u. changes the position of the Cooper minimum by half a p -state interval. It is therefore fair to claim insensitivity to this parameter.

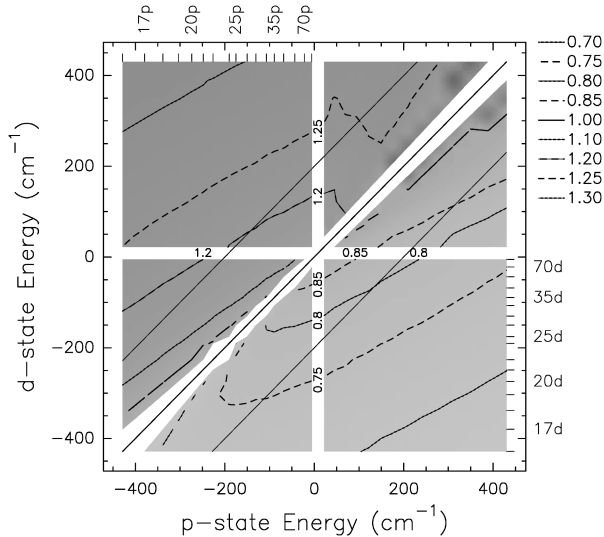
The dependence on the quantum defect is shown in Fig. 2: We have shifted the quantum defect of the Li $21s$ state by 10^{-3} and observe a slight shift in the position of the Cooper minimum. The Cooper minimum shifts almost linearly with the quantum defect. The p -state energy shifts 8.0 cm^{-1} per 10^{-3} quantum defect change in the s state, while the s -state energy shifts 18.7 cm^{-1} per 10^{-3} quantum defect change in the p state. In [43], the quantum defects are given with an accuracy in the 10^{-5} range, so that the inaccuracies due to the quantum defects are small, too.

VI. HYDROGEN

We first present the matrix-elements of hydrogen, and show the simple scaling of these matrix elements. Exact analytical formulas for these matrix elements exist, but are cumbersome to evaluate [29]. We have selected some transitions, and found that the relative difference between these exact formulas and our calculations was less than 10^{-5} . Our aim therefore is to assess the accuracy of the much simpler semiclassical matrix elements of Eqs. (10) and (11) and to describe the deviations from these formulas.

Figures 3–5 show the matrix elements of transitions between several hydrogenic states. Figure 3, for example, shows the transitions between hydrogen s and p states. The binding energy of the s states is represented by the horizontal axis, with markings for the bound states that are included in the calculations atop. Similarly, the vertical axis shows the p -state binding energy. The relative dipole matrix elements (see Sec. IV) are plotted as contours (which are chosen for each figure) and gray shades (the same for all figures).

The horizontal and vertical white spaces between the gray areas are the regions near the ionization thresholds of the s

FIG. 4. Hydrogen p - d relative dipole matrix elements.

and p series. The grid size determined the closest states to the threshold. At the middle diagonal, the binding energies of the s and the p states are equal. This space marks the boundary between the $\Delta l = +1$ and $\Delta l = -1$ regions. The matrix elements at this diagonal are best described by the size of the Rydberg orbit ($\langle r \rangle \sim \omega^{-1}$). Equation (10) diverges, however, and we have discarded these points from the figures.

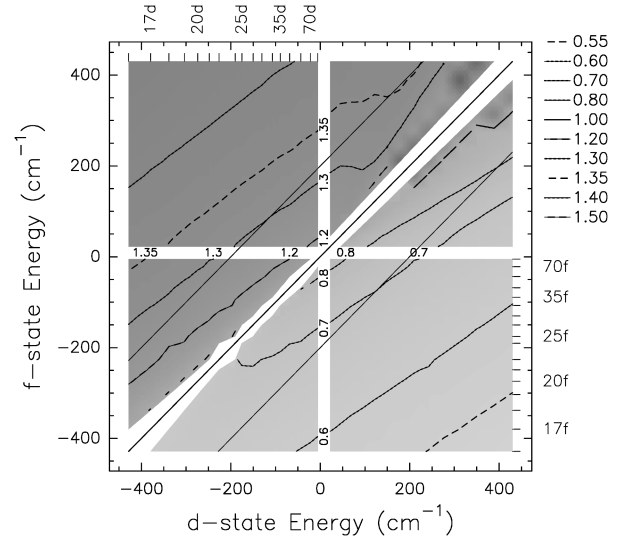
Two more diagonal lines are added to guide the eye: The upper diagonal shows the $\Delta l = +1$ transitions at $\omega = 200 \text{ cm}^{-1}$, where the p state has a higher binding energy than the s state. Similarly, the $\Delta l = -1$ transitions at $\omega = 200 \text{ cm}^{-1}$ are shown by the lower diagonal.

Starting with the d - f transitions (Fig. 5), we see that the scaling with the “lowest-order approximation” [32] in Eq. (22) reduces the dynamic range of the graph from orders of magnitude of the unscaled matrix elements to less than a factor of 2. The $\Delta l = +1$ transitions are clearly favored, over the $\Delta l = -1$ transitions. The deviations scale mainly with the transition frequency: the contours in Fig. 5 run almost parallel to the diagonals. At the $\omega = 200 \text{ cm}^{-1}$ diagonals, the relative matrix elements are 1.3 for the higher and 0.7 for the lower diagonal. Higher-order semiclassical theory for $l^3\omega = 5400 \text{ cm}^{-1}$ [Eq. (11) and Fig. 1] yields the same result.

For the upper-left corner, $l^3\omega$ becomes so large that higher-order terms in the power expansion of Eq. (13) become important. Taking only the first two terms for C_+ (“first-order approximation” from Ref. [32]) overestimates the matrix elements.

For the p - d transitions (shown in Fig. 4), the difference between $\Delta l = +1$ and $\Delta l = -1$ transitions is less pronounced. According to the semiclassical theory the relative matrix element at 200 cm^{-1} ($l^3\omega = 1600 \text{ cm}^{-1}$ in Fig. 1) should be 1.2 for the higher and 0.8 for the lower diagonal. Although the 1.2 and 0.8 contours cross the 200 cm^{-1} diagonals in Fig. 4, these seem no longer the best description.

Higher-order correction is even less needed for the s - p transitions (shown in Fig. 3). In this range, the matrix elements deviate less than 15% from Eq. (10) scaling canceled by Eq. (22). Equation (11) and Fig. 1, however, do not describe this deviation very well: The contours no longer run parallel to the diagonals, and the deviations are thus depen-

FIG. 5. Hydrogen d - f relative dipole matrix elements.

dent on both the energies of the s and p state.

The semiclassical approximations that are used for Eq. (11) are best at these intermediate values of l : For very low l , deviations of the wave function near the core contribute, while for high l ($l \sim n$) the radial and angular motion are no longer independent. From Eq. (11) contours that run parallel to the diagonals are expected, as the values within one graph only depend on the transition frequency. Comparing Figs. 3–5 this trend is visible, and for higher l (not shown) the agreement is even better.

Finally, we have compared the presented results with the higher-order semiclassical theory of Eq. (11). Far from the diagonals, they agree within 2%. In the (lower-left) bound-bound region of the figures, the combination of Eq. (10) and Eq. (11) overestimates the matrix elements. This deviation is due to the breakdown of Eq. (9) of neighboring states, as discussed below Eq. (9). In the (upper-right) free-free region of the figures, two effects play a role: towards the diagonal, the matrix elements increase and become less dependent on l , as the regime where Eq. (14) holds is approached.

Upon inspection of Figs. 3–5, one can interpret the two regimes for the dipole matrix elements in another way as well. Whenever Eq. (11) predicts large differences between the $\Delta l = +1$ and $\Delta l = -1$ transitions, as for the d - f transitions, the figure shows contours that are almost diagonal, as expected. For the s - p transitions, however, the contours become horizontal, and the *higher- l* state mostly determines the relative matrix element.

Example cross-section calculation

With the values from Figs. 3–5, the cross sections for ionization of any Rydberg state are readily evaluated, using Eqs. (1), (5), and (22). We discuss as an example the ionization of the hydrogen $27s$ state with $50 \mu\text{m}$ linearly polarized light. From Fig. 3 the relative matrix element for the $27s$ state (at -150 cm^{-1}) to a p -continuum state at 50 cm^{-1} is found to be 1.10. We first multiply this with 0.4108, the prefactor from the denominator of Eq. (22), square the result, and multiply with the angular part of the dipole matrix ele-

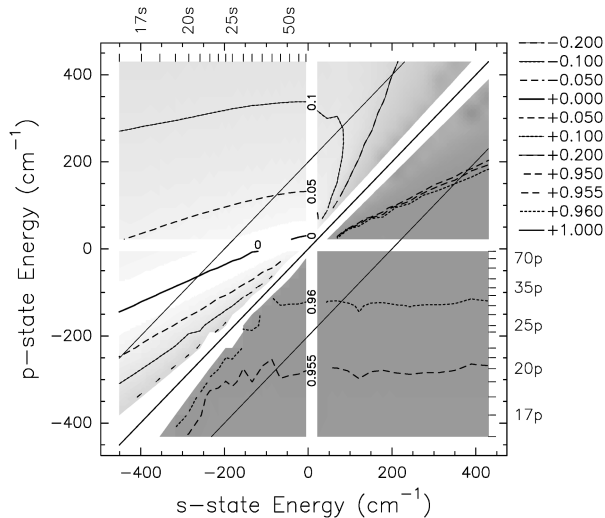


FIG. 6. Lithium s - p relative dipole matrix elements.

ment for linearly polarized light as given by Eq. (5): $(1.10 \times 0.4108)^2 \times 1/3 = 0.068$. The frequency-dependent contributions from the denominator of Eq. (22) are the binding energy of the s state, ω_n (-150 cm^{-1}), and the transition frequency ω (200 cm^{-1}). Because the final state is free, the $\omega_{n'}$ term should be set to 1. The frequency-dependent parts are squared, and the result is multiplied by the photon energy to include the ω term from Eq. (1). After the conversion of the frequencies to atomic units, this reads $(300/219\,372)^{3/2} \times 1 \times (200/219\,372)^{-7/3} = 627.5$. The cross section in atomic units is therefore $0.096\,05 \times 0.068 \times 627.5 = 4.1$. This is equivalent to $4.1 \times (5.2917 \times 10^{-9})^2 = 1.15 \times 10^{-16} \text{ cm}^2$. The conversion of radial matrix elements to a cross section was verified with the formulas from Ref. [44].

VII. LITHIUM

Lithium has very interesting properties at the wavelengths under study. The quantum defects in Table I already give some hints of these features. First of all, only the s states have an appreciable quantum defect. As the quantum defect of the s states is almost a half, the wave functions of the s states are shifted by almost π compared to the other series: The s states' wave functions mainly contain irregular Coulomb functions, while the other l states mainly contain regular Coulomb functions. The dipole matrix elements between s and p states reflect this particular configuration.

Two features dominate the relative matrix elements of the high-lying s - p transitions, as shown in Fig. 6: The large difference between the $\Delta l = +1$ and the $\Delta l = -1$ transition matrix elements, and the zero in the matrix elements in the $\Delta l = +1$ region. The wavelength of this Cooper minimum changes with the binding energy, as will be discussed in Sec. X. To assess the sensitivity of the Cooper minimum on the fine structure, we have changed the quantum defect of the p state with a full fine structure difference in both directions, and observed no difference to the results on the scale in Fig. 6. For s states bound with less than -120 cm^{-1} , the Cooper minimum exists in ns - ϵp transitions, while for deeper bound s states the Cooper minimum appears in the transitions to bound p states. The zero crossing is the continuation of the minimum in the cross sections starting from lower n : Matrix

TABLE III. Lithium: Relative dipole matrix elements for excitation of states at -200 cm^{-1} to the threshold.

	$\Delta l = +1$		$\Delta l = -1$		$\cos \Delta \nu_l$
	Calculated	Eq. (15)	Calculated	Eq. (15)	
s - p	0.02	-0.07	0.96	0.96	0.45
p - d	1.12	0.91	0.86	1.07	0.99

elements between the $2s$ ground state and the excited np states are much smaller than their hydrogenic equivalents. The $2s$ - $2p$ and $2s$ - $3p$ transitions are most reduced, and evaluation of the wave functions showed that the matrix elements change sign between the $2p$ and $3p$ states [45]. Due to these reduced matrix elements, the lifetimes of the low-lying p states are orders of magnitude larger than those of equivalent states in other elements [18,46]: In contrast with most atoms, the p states mainly decay to d states instead of s states [18].

Because of its abundance in stars, many of the strengths of transitions between low-lying ($n \leq 10$) states are known [47-49]. A careful inspection of these values and those from [18] reveals that minima in the oscillator strength exist for these $n's$ - np , $n' < n$ transitions. Because of the small core of lithium, quantum defect theory agrees well with cross sections for low n that are obtained with more elaborate calculation methods [6]. Our calculations are in agreement with the tabulated values from [18].

Table III summarizes these numerically calculated relative matrix elements for photoabsorption by states that are bound with -200 cm^{-1} to states near the ionization threshold. These values are compared with the results of two formulas for free-free matrix elements. The first two pairs of columns contain the numerically calculated matrix element, and the result Eq. (15) divided by 0.4108, using the quantum defects from Table I. Equation (15) shows, like the numerical calculations, a disparity of the $\Delta l = +1$ and $\Delta l = -1$ s - p transitions. The values deviate strongly from the hydrogenic values. In the last column, the cosine of the quantum defect difference is given: for free-free matrix elements the relative matrix elements approach this value as $\omega \ll E$.

A plot for the p - d transitions (not shown) resembled the hydrogenic results as shown in Fig. 4. As indicated by the values in Table III, the cross sections at the threshold deviate little from the hydrogenic values of 1.2 and 0.8 (cf. Fig. 4). The analytical approximations do not reflect this Bethe rule behavior as expressed in Eq. (11). The similarity of the graphs for lithium and hydrogen indicates that the quantum defect difference is small enough to prefer Eq. (11) over Eq. (15) for free-free transitions.

The other lithium transitions, involving higher-angular-momentum states, are indistinguishable from hydrogenic, due to the even smaller quantum defects.

VIII. RUBIDIUM

In this section we present the dipole matrix elements for the s - p , p - d , and d - f transitions in rubidium. We have chosen rubidium as the model atom because of the availability of experiments [14-16] and because the low-lying transitions deviate strongly from hydrogen. The general

TABLE IV. Rubidium: Relative dipole matrix elements for excitation of states at -200 cm^{-1} to the threshold.

	$\Delta l = +1$		$\Delta l = -1$		$\cos\Delta_l$
	Calculated	Eq. (15)	Calculated	Eq. (15)	
$s-p_{1/2}$	-0.45	-0.50	0.70	0.65	0.07
$s-p_{3/2}$	-0.49	-0.54	0.66	0.61	0.03
$p_{1/2}-d$	-0.32	-0.09	-0.99	-1.04	-0.57
$p_{3/2}-d$	-0.37	-0.14	-1.00	-1.06	-0.60
$d-f$	-0.38	-0.01	-0.92	-1.00	-0.51
$f-g$	1.36	0.97	0.62	1.03	1.00

observations found for rubidium are used in the brief descriptions of the other alkali-metal atoms in the next section.

Table IV presents some values of the relative matrix elements. A first observation is that up to the $d-f$ transitions, the dipole matrix elements do not obey the Bethe rule: In rubidium, $\Delta l = -1$ transitions are more likely than $\Delta l = +1$ transitions. The results of the $\Delta l = -1$ transitions are reasonably described by Eq. (15), but the $\Delta l = +1$ transitions deviate strongly. The absolute values of the $\Delta l = +1$ transitions are much smaller than 1, indicating that these transitions are less likely than comparable hydrogenic transitions. For higher l , the results are hydrogenic, and the prefactors are well described by Eq. (11) (Fig. 1). Secondly, the difference in quantum defects due to the fine structure splitting (1.3%) affects both the analytical and the numerical results for transitions with p states. In the remainder of this section, we present the wavelength dependence of the matrix elements for the higher fine structure levels of the l states. The values of the lower fine structure levels (not shown) are well approximated by multiplying the values from the figures with the ratios from Table IV.

Figure 7 shows the relative matrix elements for the $s-p_{3/2}$ transitions. The contours of the $\Delta l = +1$ transitions deviate most from those of hydrogen: First of all, the values are negative. This indicates that a Cooper minimum exists at higher energy [25]. Secondly, the magnitude of the matrix elements decreases and the contours become more horizontal as the p -state energy increases. As discussed in Sec. X, the

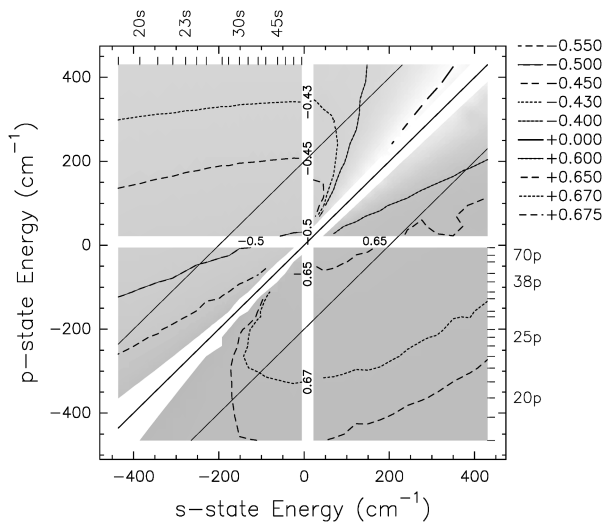


FIG. 7. Rubidium $s-p_{3/2}$ relative dipole matrix elements.

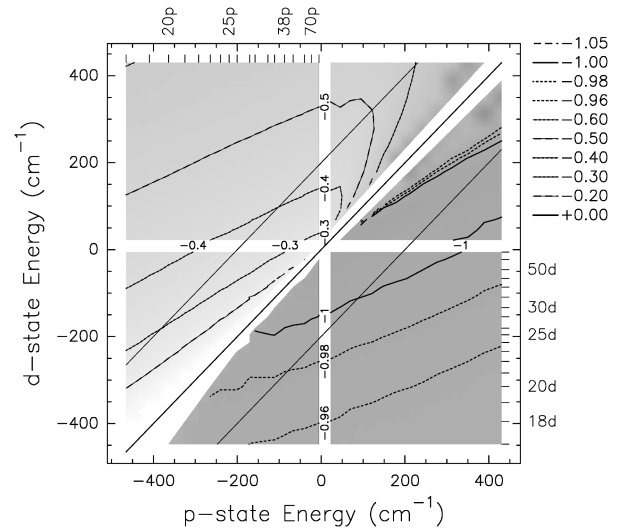


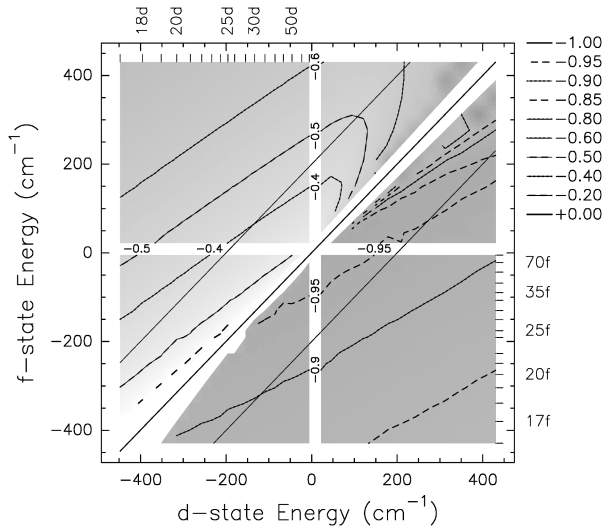
FIG. 8. Rubidium $p_{3/2}-d$ relative dipole matrix elements.

Cooper minimum only depends on the p -state energy and thus exhibits a horizontal contour. As the Cooper minimum is approached for higher energies, the slopes of the contours flatten similarly. The free-free $\Delta l = +1$ matrix elements change sign just before the middle diagonal, as indicated by the zero contour. This feature is also described in Sec. X. The matrix elements nearest to the diagonal are all positive.

The $\Delta l = -1$ matrix elements are smaller than the comparable hydrogenic ones. In the $\epsilon p-n s$ transitions, the relative matrix elements increase from 0.65 to 0.68 as the transition frequency is increased. This is different from the hydrogenic case, where, at higher energy, the $\Delta l = -1$ matrix elements decrease (cf. Fig. 1). The positive sign of the $\Delta l = -1$ matrix elements in Fig. 7 shows that no Cooper minimum exists at very high energies.

The relative change of the $\Delta l = +1$ $p-d$ transitions (Fig. 8) as a function of the transition frequency is much faster than for hydrogen. Not visible on this scale, a Cooper minimum exists for the very high-lying, bound states: For $30 < n < 70$, the transitions from np to $(n-1)d$ and nd (both are $\Delta l = +1$ due to the quantum defects) have a positive sign, while all other matrix elements are negative. For lower n , only the np to $(n-1)d$ transitions have this opposite sign, while for higher n the range extends, even though the transition frequencies for the Cooper minimum decrease. Figure 8 shows the rapid increase in cross sections away from the Cooper minimum. The matrix elements for the $\Delta l = -1$ part of the graph are somewhat higher than those of hydrogen (cf. Fig. 8), and are somewhat flatter. The relative matrix elements for $\omega = 200 \text{ cm}^{-1}$ are maximal near the threshold between bound-free and bound-bound transitions. For $\omega \sim E$, the matrix elements decrease as the conditions for Eq. (14) are met.

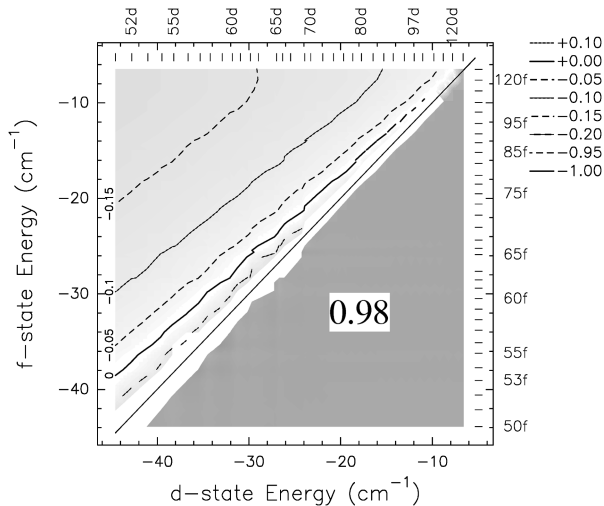
The $d-f$ transitions shown in Fig. 9 resemble the $p-d$ transitions in many respects. The quantum defect differences are in both cases approximately 1.3, resulting in similar analytical and the numerical values (Table IV). Figure 9 shows that the $\Delta l = -1$ transitions share the wavelength dependence, even though the values for $d-f$ are close to 0.9 rather than 1. Again a maximum occurs just above the threshold between bound-free and free-free transitions.

FIG. 9. Rubidium d - f relative dipole matrix elements.

The $\Delta l = +1$ d - f transitions again show a rapid increase as the transition frequency increases. As for the p - d transitions, this is due to a Cooper minimum near the diagonal. This Cooper minimum, however, is at slightly higher photon energy: Starting from the diagonal, the first three or four states have the positive sign. Figure 10 shows the transition matrix elements for the *bound-bound* Rb d - f transitions in more detail. For $n \sim 50$, the Cooper minimum occurs at a photon energy of 6 cm^{-1} . The Cooper minimum slowly approaches the diagonal for higher bound states.

IX. OTHER ALKALI-METAL ATOMS

In this section we present the relative dipole matrix elements for the excitation of Rydberg states to the ionization threshold with $50 \mu\text{m}$ radiation. Whenever the dipole matrix elements are very small, the matrix elements around the accompanying Cooper minimum are shown. Note that all these alkali-metal atoms have a Cooper minimum in the cross sections for ionization of their ns ground states [50]. These

FIG. 10. Rubidium d - f relative dipole matrix elements for transitions between very high-lying, bound states.TABLE V. Sodium: Relative dipole matrix elements for excitation of states at -200 cm^{-1} to the threshold.

	$\Delta l = +1$		$\Delta l = -1$		$\cos\Delta_l$
	Calculated	Eq. (15)	Calculated	Eq. (15)	
s - p	-0.50	-0.56	0.65	0.60	0.02
p - d	-1.25	-1.15	-0.37	-0.60	-0.88
d - f	1.28	0.97	0.71	1.02	1.00

ground-state Cooper minima are well studied both experimentally and theoretically [50,51].

A. Sodium

The sodium s - p transitions are much like those of rubidium: A Cooper minimum, relatively high in the continuum, changes the sign of the $\Delta l = +1$ transitions, and causes them slowly to decrease. Neither the matrix elements p - d nor the d - f transitions show remarkable features. All p - d transitions have negative, while all d - f transitions have positive, matrix elements. (See Table V.)

B. Potassium

Potassium has, like the other alkali-metal atoms, an $s \rightarrow p$ Cooper minimum far in the continuum. The p - d transitions, however, are more interesting: A Cooper minimum in the bound-free transitions for the $\Delta l = +1$ transitions appears near 300 cm^{-1} . Figure 11 shows the relative matrix elements, on a scale that is extended further into the continuum than the other plots in this paper. The position of Cooper minimum depends strongly on the initial-state energy. The characteristic bend in the free-free regime is discussed in Sec. X. The d - f transitions in potassium show no particularities: All values are positive, and the values change smoothly. (See Table VI.)

C. Cesium

Cesium Rydberg transitions are studied by Lahiri and Manson [25]. As cesium is the heaviest atom we study, the fine structure splittings affect the matrix elements most for this atom.

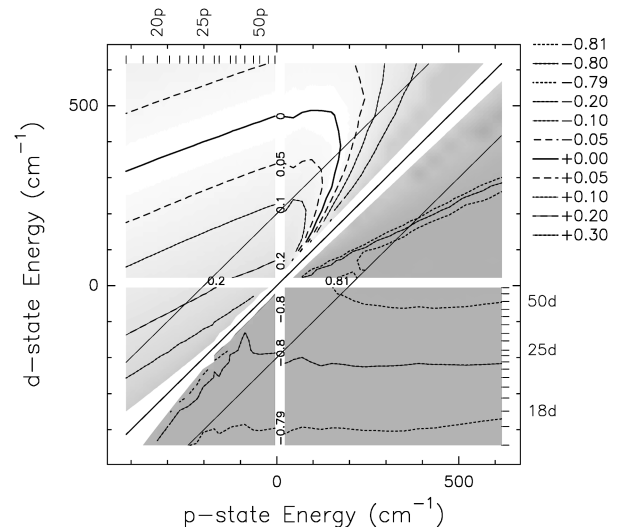
FIG. 11. Potassium $p_{3/2}$ - d relative dipole matrix elements.

TABLE VI. Potassium: Relative dipole matrix elements for excitation of states at -200 cm^{-1} to the threshold.

	$\Delta l = +1$		$\Delta l = -1$		$\cos\Delta_l$ Eq. (14)
	Calculated	Eq. (15)	Calculated	Eq. (15)	
$s-p_{1/2}$	-0.41	-0.47	0.72	0.68	0.11
$s-p_{3/2}$	-0.43	-0.48	0.72	0.67	0.10
$p_{1/2}-d$	0.20	0.37	-0.80	-0.76	-0.20
$p_{3/2}-d$	0.19	0.36	-0.80	-0.77	-0.21
$d-f$	0.63	0.24	0.95	1.10	0.67
$f-g$	1.37	0.98	0.60	1.02	1.00

Table VII shows again some of the calculated matrix elements. Like the other alkali-metal atoms, a Cooper minimum in the continuum reduces the ionization cross sections of the $s-p$ transitions near the threshold. In the entire range of our calculations, the $p-d$ dipole matrix elements are negative and vary slowly. The $\Delta l = -1$ matrix elements are somewhat enhanced compared to hydrogen.

The $d-f$ transitions, however, exhibit a Cooper minimum (Fig. 12). The $d-f$ transitions exhibit multiple Cooper minima [25]. For the lower states, the positions of these Cooper minima are difficult to calculate, and results obtained by different methods disagree [52]. Quantum defect theory, however, is appropriate for the highly excited states we study.

X. DISCUSSION

We discuss some of the features that are found in the calculations for the alkali-metal atoms. First of all, we distinguish two regimes. The dipole matrix elements are either well described by the Bethe rule formula Eq. (11), or dominated by other factors. These factors are either that l is too low for the semiclassical formula to apply [e.g., the H $s-p$ transitions (Fig. 3)] or that strong deviations from the hydrogenic case exist, due to the difference quantum defects, as for the low- l alkali-metal states. If these other factors dominate, the contours are flatter. In other words, the energy of the *higher- l* state mostly determines the relative matrix element. This can be understood as follows: The outer part of the bound wave function hardly contributes to the dipole matrix

TABLE VII. Cesium: Relative dipole matrix elements for excitation of states at -200 cm^{-1} to the threshold.

	$\Delta l = +1$		$\Delta l = -1$		$\cos\Delta_l$ Eq. (14)
	Calculated	Eq. (15)	Calculated	Eq. (15)	
$s-p_{1/2}$	-0.39	-0.44	0.75	0.70	0.13
$s-p_{3/2}$	-0.50	-0.55	0.66	0.61	0.03
$p_{1/2}-d_{3/2}$	-0.95	-0.73	-0.96	-1.14	-0.93
$p_{3/2}-d_{3/2}$	-1.03	-0.82	-0.92	-1.12	-0.97
$p_{3/2}-d_{5/2}$	-1.01	-0.79	-0.93	-1.12	-0.96
$d_{3/2}-f$	-0.09	-0.39	0.78	0.75	0.18
$d_{5/2}-f$	-0.05	-0.35	0.79	0.77	0.21
$f-g$	1.35	0.93	0.66	1.06	0.99

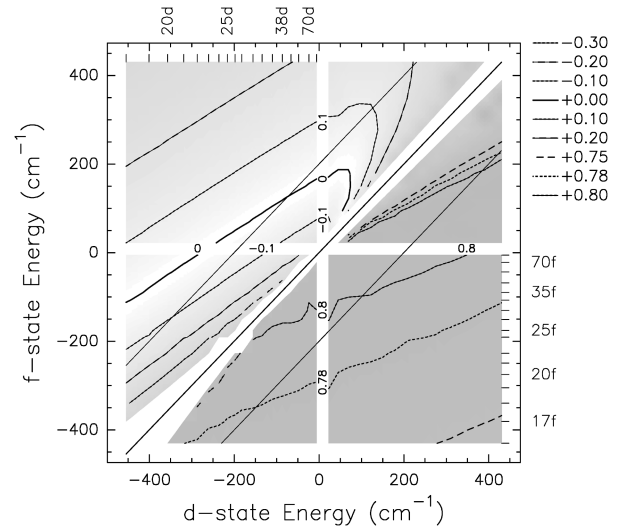


FIG. 12. Cesium $d_{5/2}-f$ relative dipole matrix elements.

elements, as the continuum wave function oscillates more rapidly than the bound state. The computed matrix element is therefore mainly determined at the small- r end point of the integration of Eq. (4). This end point is determined by the inner turning point of the higher- l state. The energy of the higher- l state is therefore most important for the matrix elements. The Rb $s-p$ transitions (Fig. 7) clearly show this dependence.

The exclusive dependence on the high- l -state energy does not hold for small ω : If the local k vectors of both wave functions become comparable, a large r range of the wave function contributes to the matrix element. In that case, both wave functions oscillate at approximately the same frequency, and contributions from the remote area are important. At a Cooper minimum at small ω , contributions from the range near the core and the remote wave function must cancel each other. Upon changing the energy of one of the states, the other has to be shifted by approximately the same amount to retain this cancellation. The position of the Cooper minimum therefore depends on the *transition frequency* rather than on the binding energy of either state. This behavior is found for the Rb $d-f$ transitions (Fig. 10), where the Cooper minimum runs almost diagonally.

Finally, we want to discuss the “bend” in the Cooper minima in the free-free regime, as found in the K $p-d$ (Fig. 11) and Cs $d-f$ (Fig. 12) transitions. The shape can be understood from the continuity of the matrix elements as a function of the initial- and final-state energy. For small ω , the matrix elements are described by Eq. (14). Near $\omega \sim E$ this must pass smoothly into the regime in which Eq. (15) is valid. The bend of the Cooper minimum occurs in this transition regime. Taking the example of the K $p-d$ transitions (Table VI and Fig. 11) the matrix elements are positive near the diagonal in the free-free regime. At $E=0$, the zero contour points a little away from the diagonal, near the half angle of the diagonal, where $\omega \sim E$. With the bend at a p -state energy of 200 cm^{-1} , it connects to the bound-free Cooper minimum at the threshold d -state energy of 500 cm^{-1} . The zero near the diagonal of the free-free Rb $s-p$ transitions (Fig. 7) is a remnant of a similar bend. We have calculated (not shown) the matrix elements of the low-lying

s-p transitions in the alkali-metal atoms near their Cooper minima. The characteristic bend occurred in all these calculations.

The semiclassical formulas [Eqs. (14) and (15)] also predict the existence of Cooper minima: It has been assumed [25] that all matrix elements should be positive for high energies. Negative matrix elements therefore imply that a Cooper minimum exists at higher free energy. We can now refine this rule, since we have numerically shown that Cooper minima exist whenever the sign is opposite to the result of Eq. (14). When Eq. (15) and Eq. (14) yield opposite signs, a Cooper minimum exists.

ACKNOWLEDGMENTS

We would like to thank H. G. Muller for his assistance with the calculations and H. B. van Linden van den Heuvell, S. Woutersen, M. Drabbels, F. Robicheaux, and N. B. Delone for fruitful discussions and a careful reading of the manuscript. The work described in this paper is part of the research program of the Stichting Fundamenteel Onderzoek van de Materie (Foundation for Fundamental Research on Matter), and was made possible by financial support from the Nederlandse Organisatie voor Wetenschappelijk Onderzoek (Netherlands Organization for the Advancement of Research).

-
- [1] T. F. Gallagher, *Rydberg Atoms* (Cambridge University Press, Cambridge, England 1994).
- [2] R. G. Rolfes, L. G. Gray, O. P. Makarov, and K. B. MacAdam, *J. Phys. B* **26**, 2191 (1993).
- [3] I. E. McCarthy, K. Ratnavelu, and Y. Zhou, *J. Phys. B* **26**, 2733 (1993).
- [4] C. K. Kwan, W. E. Kauppila, R. A. Lukaszew, S. P. Parikh, T. S. Stein, Y. J. Wan, and M. S. Dababneh, *Phys. Rev. A* **44**, 1620 (1994).
- [5] S. Wane, *J. Phys. B* **18**, 3881 (1985).
- [6] J. Lahiri and S. T. Manson, *Phys. Rev. A* **48**, 3674 (1993).
- [7] E. J. Beiting, G. F. Hildebrandt, F. G. Kellert, G. W. Foltz, K. A. Smith, F. B. Dunning, and R. F. Stebbings, *J. Chem. Phys.* **70**, 3551 (1979).
- [8] T. F. Gallagher and W. E. Cooke, *Appl. Phys. Lett.* **34**, 369 (1979).
- [9] W. E. Cooke and T. F. Gallagher, *Phys. Rev. A* **21**, 588 (1980).
- [10] H. Figger, G. Leuchs, R. Straubinger, and H. Walther, *Opt. Commun.* **33**, 37 (1980).
- [11] T. W. Ducas, W. P. Spencer, A. G. Vaidyanathan, W. H. Hamilton, and D. Kleppner, *Appl. Phys. Lett.* **35**, 382 (1979).
- [12] C. E. Burkhardt, M. Ciocca, J. J. Leventhal, E. Arimondo, T. Bergeman, and S. T. Manson, *Nucl. Instrum. Methods Phys. Res. B* **56**, 313 (1993).
- [13] J. H. Hoogenraad, R. B. Vrijen, A. F. G. van der Meer, P. W. van Amersfoort, and L. D. Noordam, *Phys. Rev. Lett.* **75**, 4579 (1995).
- [14] J. H. Hoogenraad, R. B. Vrijen, and L. D. Noordam, following paper, *Phys. Rev. A* **57**, 4546 (1998).
- [15] R. B. Vrijen, D. I. Duncan, and L. D. Noordam, *Phys. Rev. A* **56**, 2205 (1997).
- [16] G. M. Lankhuijzen, M. Drabbels, F. Robicheaux, and L. D. Noordam, *Phys. Rev. A* **57**, 440 (1998).
- [17] H. A. Bethe and E. E. Salpeter, *Quantum Mechanics of One- and Two-Electron Atoms* (Plenum, New York, 1977).
- [18] A. Lindgård and S. E. Nielsen, *At. Data Nucl. Data Tables* **19**, 533 (1977).
- [19] C. E. Theodosiou, *Phys. Rev. A* **30**, 2881 (1984).
- [20] J. W. Cooper, *Phys. Rev.* **128**, 681 (1962).
- [21] H. Park and R. N. Zare, *Chem. Phys. Lett.* **225**, 327 (1994).
- [22] W. A. Chupka, *J. Chem. Phys.* **87**, 1488 (1987).
- [23] K. Wang, J. A. Stephens, and V. McKoy, *J. Phys. Chem.* **97**, 9874 (1993).
- [24] M. Aymar, E. Luc-Koenig, and F. Combet Farnoux, *J. Phys. B* **9**, 1279 (1976).
- [25] J. Lahiri and S. T. Manson, *Phys. Rev. A* **33**, 3151 (1986).
- [26] N. B. Avdonina and M. Y. Amusia, *J. Phys. B* **16**, L543 (1983).
- [27] N. B. Delone, S. P. Goreslavsky, and V. P. Krainov, *J. Phys. B* **27**, 4403 (1994).
- [28] B. Kaulakys, *J. Phys. B* **28**, 4963 (1995).
- [29] W. Gordon, *Ann. Phys. (Leipzig)* **2**, 1031 (1929).
- [30] S. P. Goreslavskiĭ, N. B. Delone, and V. P. Krainov, *Zh. Éksp. Teor. Fiz.* **82**, 1789 (1982) [*Sov. Phys. JETP* **55**, 1032 (1982)].
- [31] I. Y. Berson, *Zh. Éksp. Teor. Fiz.* **83**, 1276 (1982) [*Sov. Phys. JETP* **56**, 731 (1982)].
- [32] M. S. Adams, M. V. Fedorov, V. P. Krainov, and D. D. Meyerhofer, *Phys. Rev. A* **52**, 125 (1995).
- [33] M. J. Seaton, *Mon. Not. R. Astron. Soc.* **118**, 504 (1958).
- [34] M. J. Seaton, *Rep. Prog. Phys.* **46**, 167 (1983).
- [35] V. A. Davydkin and B. A. Zon, *Opt. Spectrosc.* **51**, 25 (1981) [*Opt. Spectrosc.* **51**, 13 (1981)].
- [36] B. Oumarou, J. Picart, N. Tran Minh, and J. Chapelle, *Phys. Rev. A* **37**, 1885 (1988).
- [37] N. B. Delone, S. P. Goreslavsky, and V. P. Krainov, *J. Phys. B* **22**, 2941 (1989).
- [38] M. Trippenbach, K. Rzażewski, M. V. Fedorov, and A. E. Kazakov, *J. Phys. B* **22**, 1193 (1989).
- [39] M. L. Zimmerman, M. G. Littman, M. M. Kash, and D. Kleppner, *Phys. Rev. A* **20**, 2251 (1979).
- [40] W. P. Spencer, A. G. Vaidyanathan, D. Kleppner, and T. W. Ducas, *Phys. Rev. A* **26**, 1490 (1982).
- [41] L. V. Chernysheva, N. A. Cherepkov, and V. Radojević, *Comput. Phys. Commun.* **11**, 57 (1976).
- [42] H. G. Muller, Ph.D. thesis, Vrije Universiteit Amsterdam, 1985.
- [43] C.-J. Lorenzen and K. Niemax, *Phys. Scr.* **27**, 300 (1983).
- [44] M. Aymar, O. Robaux, and S. Wane, *J. Phys. B* **17**, 993 (1984).
- [45] U. Fano and J. W. Cooper, *Rev. Mod. Phys.* **40**, 441 (1968).
- [46] C. E. Theodosiou, L. J. Curtis, and M. El-Mekki, *Phys. Rev. A* **44**, 7144 (1991).
- [47] T. C. Caves and A. Dalgarno, *J. Quant. Spectrosc. Radiat. Transf.* **12**, 1539 (1972).
- [48] G. Peach, H. E. Saraph, and M. J. Seaton, *J. Phys. B* **21**, 3669

- (1988).
- [49] W. Cunto, C. Mendoza, F. Ochsenbein, and C. J. Zeippen, *Astron. Astrophys.* **275**, L5 (1993).
- [50] G. Baum, M. S. Lubell, and W. Raith, *Phys. Rev. A* **5**, 1073 (1972).
- [51] Y.-Y. Yin and D. S. Elliott, *Phys. Rev. A* **46**, 1339 (1992).
- [52] A. Z. Msezane and S. T. Manson, *Phys. Rev. A* **29**, 1594 (1984).